SEM Image-based Porosity Analysis of Fire Damaged High Strength Concrete

Diana A. Andrushia[1], N. Anand[2*], Éva Lublóy[3*], M. Z. Naser[4], Balamurali Kanagaraj[2]

[1] Department of ECE, Karunya Institute of Technology and Sciences, Karunya Nagar, 641114, Coimbatore, India
[2] Department of Civil Engineering, Karunya Institute of Technology and Sciences, Coimbatore, Karunya Nagar, 641114, India
[3] Department of Construction Materials and Technologies, Faculty of Civil Engineering, Budapest University of Technology and Economics, Műegyetem rkp. 1–3, Budapest, 1111, Hungary
[4] School of Civil and Environmental Engineering & Earth Sciences, Clemson, SC 29634, United States
* Corresponding author, e-mail: lubloy.eva@emk.bme.hu; nanand@karunya.edu

Abstract

The porosity of concrete affects the durability of reinforced concrete structures, wherein high levels of porosity are linked to a shorter service life. Recent works have noted that high porosity levels naturally exist in the aftermath of a fire exposure – especially when concrete is classified as high strength concrete (HSC). To shed more light into this phenomenon, this paper showcases a method for measuring the porosity of HSC under elevated temperatures through scanning electron microscopy (SEM). In this method, SEM-based images were examined to quantify the surface porosity of fire-affected HSC. Detailed image analysis was performed for HSC exposed to various heating durations. The study concludes that the surface porosity obtained via the SEM processing method is in good agreement with that from the SEM-based method (with a minor average difference of 3.8%). As such, the proposed method is expected to be reliable for the porosity analysis of fire-damaged concrete.

Keywords

SEM, image analysis, elevated temperature, porosity, high strength concrete

1 Introduction

High strength concrete (HSC) is a dense and an impervious construction material with higher strength and long serviceability and hence is widely preferred for the construction of infrastructures. In the event of a fire, the material properties of HSC degrade, and temperature-induced changes adversely affect the microstructure of HSC, which also negatively affect the porosity of concrete by inducing micro- and macro-sized cracks and pores. Since the load carrying capacity of reinforced concrete (RC) elements are closely linked with the mechanical properties of concrete (including porosity), then examining the porosity of fire-affected HSC is of importance.

Various methods are available in design standards to measure the porosity of construction materials [1]. Water permeability, sorptivity, and water absorption are some of the conventional experimental methods used to determine the porosity of concrete [2]. These methods provide information about the porosity of concrete, and they depend on many parameters such as strength grade, type of cement/

admixtures, type of concrete, etc. [3]. However, such methods require specialized equipment and hence are costly and may not be readily available [4]. On the other hand, image-based analysis of porosity requires reduced amount of time and effort [5]. This, it is a preferable analytical method to study in-depth the behavior and nature of pores. The effect of porosity and the related strength of concrete depends on the geometry, structure, density, and connectivity in the micro-structure [6].

Fire-affected concrete exhibits higher compressive strength loss and higher porosity than concrete under ambient conditions. Former studies indicated that the damage level in terms of porosity is higher for concrete with higher strength [7]. The porous morphology is extremely complex in the fire-affected concrete. Recently, digital image processing-based methods have been leveraged to study porosity distribution and total porosity of concrete. Few researchers have used porosity analysis using the SEM images technique to study the porosity of different

concrete types [8, 9]. SEM images are used to segment the porosity of powder concrete. The threshold-based method is adopted to classify the SEM images [8].

Image analysis provides representative and reproducible data which can be used to study the behavioral characteristics of fire-affected concrete. For instance, [9] used a combination of imaging techniques such as binary operations, filtering, grey-level thresholding to separate aggregate particles from cement paste in backscattered electron (BSE) images of concrete. Image analysis was used to segment the aggregate from BSE images, and thereby porosity was measured. The image-based method was adopted to find the porosity. The average porosity calculated through image analysis was compared with different volumetric methods. The image recognition technique was used to significantly analyze the micromorphology of concert samples. The correlation between compressive strength and textural features are higher than 90% [10].

The pore network of high-performance concrete (HPC) was analyzed through 3D SEM [11]. Four HPC samples are imaged in order to find pore structure. The imaging techniques of skeletonization and thresholding were used to find the pore size distribution ImageJ software with default algorithms and parameters was used to segment the pores from SEM images. The Otsu threshold algorithm produced good visualization results in comparison with other algorithms. Quantification of porosity in carbonates and aragonite sandstone was studied by [12]. The batch-based image processing techniques were successfully adopted to identify and quantify the porosity in SEM images. Low and high grey values of SEM images were taken as thresholds in order to find pores. The pore volumes were quantified through a mercury intrusion porosimeter. Table 1, describes the recent trends in concrete subjecting to temperature exposure. SEM was also used to measure the porosity of materials such as aluminum [13], cement mix [14], titanium alloy [15], and coal [16].

The determination of porosity of fire-affected concrete using SEM images is less studied in the literature. Hence, analysis of porosity of HSC under elevated temperature based on SEM images is gaining more attention in studying the changes in the behavior of microstructure of concrete paste. The main objective of this investigation is to develop an image processing-based method to quantify the surface porosity of fire-affected HSC. A secondary objective is to ensure that the developed method provides better pore detection and quantification than the conventional experimental methods. This investigation emphasizes the determination of porosity in terms of the percentage of fire-affected concrete specimens with different heating durations. SEM analysis results considered in this study are based on real experimental testing programs.

2 Experimental program and methodology
2.1 Preparation of HSC specimens
Concrete samples with a strength grade of M60 were prepared with ordinary Portland cement (53 grade), manufactured sand, granite stones, and Class F fly ash as per IS 10262:2016 [17]. The specific gravity of cement, fine and coarse aggregates were 3.15, 2.62, and 2.68, respectively. Superplasticizer was used to achieve a target slump of 100-125 mm. A series of trials were conducted to arrive at a design mix that satisfies the workability and hardened properties of concrete. Table 1 shows the mix proportion used for HSC.

A number of cube specimens of size $150 \times 150 \times 150$ mm was used to assess the compressive strength of HSC. Concrete samples were kept for curing for about 28 days, and these were kept at ± 30 °C for 48 hours before the elevated temperature test. The compressive strength of control specimens was examined and reported as 62.25 MPa. Other samples were kept in a specialized furnace and heated up to 60 ºC for 1 hour to release the absorbed water, prior to the elevated temperature testing.

Then these specimens were heated in a computer-controlled electrical furnace following the ISO834 standard fire temperature curve for two hours (Fig. 1(a)). The HSC specimens were heated for 60 min (maximum temperature of 925 ºC), 120 min (maximum temperature of 1029 ºC), 180 min (maximum temperature of 1090 ºC), and 240 min (maximum temperature of 1133 ºC).

Table 1 Details of Mix Proportion of Ingredients (kg/m³)

Binder (Cement + fly ash)	Fine Aggregate	Coarse Aggregate	w/c ratio	Superplasticizer
565	782	1256	0.34	5.52
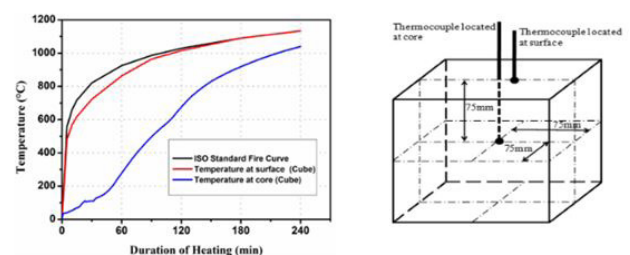
Fig. 1 (a) Time-Temperature curve, (b) locations of thermocouples in cube specimens

2.2 Heating regime of HSC specimens

The heating regime in the furnace follows the European standard temperature-time curve (ISO 834, [18]). To heat the HSC samples to the desired temperatures and duration, a digitally-controlled computerized furnace with inner dimensions of 900 mm × 500 mm × 500 mm and a power capacity of 110 kW was used. The maximum heating capacity temperature of the furnace is 1250 °C. The furnace is equipped with a microcontroller that can be programmed to control the temperature as per the standard temperature curve (Eq. (1)), as shown in Fig. 1(a).

The furnace consists of coils on four sides that heat the specimens through radiation when the target temperature is set. The furnace has two displays: a) set value display which records the specimen's temperature at different time intervals, and b) program value display which shows the coils' temperature at a given time. Thermocouples were connected to a control panel to record the temperature inside the furnace and on the test specimens (Fig. 1(b)).

After the temperature is set, the coil heats the specimens till the target time is reached, and then the furnace stops automatically (see Fig. 2). Then, the specimens are taken out from the furnace and placed in a closed area for air cooling.

3 Mechanical properties of HSC

The fresh and hardened properties of reference and heated samples are shown in Table 3. It can be seen from this table that the developed HSC satisfies the target slump and is in the range of 112–132 mm. Tests are conducted to assess the compressive and tensile strength of control specimens and concrete exposed to the standard fire. After the specified curing period, the specimens are removed from the curing environment and tested for compressive strength. The specimens are aligned properly on the testing machine's platen, ensuring even loading. A compressive force is applied gradually and uniformly to the specimen using a Compression Testing Machine (CTM). The load is applied at a constant rate until the specimen fails, typically at a loading rate of 0.2 to 0.4 MPa/second in accordance with IS 516:2004 [19].

A drop in both residual compressive and residual tensile strength was observed as the heating duration increased. The loss in the compressive strength was between 26.8% and 84.5% for the samples heated to 60 and 240 min, respectively. Also, a drastic loss in tensile strength was noted, and the loss ranged between 32.4% and 88% for the samples subjected to 60 min to 180 min heating exposure.

However, HSC 240 specimens did not sustain any loads and failed under self-weight. The disruption of CSH gel, thermal incompatibility between cement paste and aggregate and development of macrocracks are some of the reasons for the reduction in compressive strength of concrete [20]. Also, the concrete is more sensitive to tensile loading after the higher temperature exposure. As the concrete porous and damaged with microcracks under the elevated temperature, further with the application of tensile stresses the rate of reduction in tension capacity of concrete is higher as compared to compression capacity.

4 Acquisition of SEM images

A scanning electron microscope (SEM) scans a focused electron beam over a surface to create an image. The electrons in the beam interact with the sample, producing various signals that can be used to obtain information about the surface topography and composition. SEM is an ideal methodology suitable for the investigation of surface morphology and microstructure characterization. The SEM images provide data regarding the size of the grain, shape of the grain, and porosity of the sample with high resolution [21].

The SEM analysis was carried out on HSC samples to study morphology using JEOL JSM-6390 model. It is a high-performance electron microscope with a higher resolution ranging from less than 1 nm. It has a customized GUI interface in the instrument for operation. The specifications are: voltage: 0.5 to 32 kV, Magnification: X5 to 300000, Filament type: Pre-cantered W hairpin filament, Lens: Super conical type
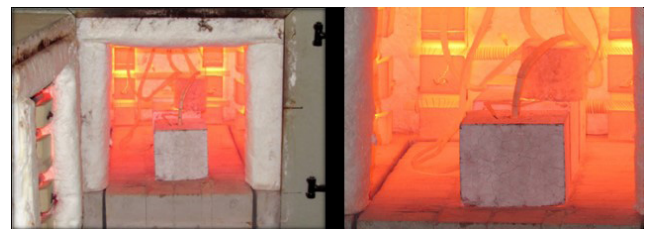
Fig. 2 View of HSC cube under temperature exposure

Table 3 Workability and Mechanical properties of HSC

Sample ID	Slump (mm)	Compressive strength (MPa)	Tensile strength (MPa)
HSC-Ref	112-132	62.25	7.22
HSC 60*	---	45.56	4.90
HSC 120	---	22.23	1.76
HSC 180	---	14.82	0.86
HSC 240	---	9.65	-

* HSC 60- High strength concrete exposed to 60 min duration

The materials were prepared on a carbon-coated copper grid by just dropping a small amount of sample (5 mg) on the grid. The excess sample was then removed, and the films on the SEM grid were allowed to dry by putting it under a mercury lamp for 5 min. The working chamber can house the specimen with a maximum diameter of 6-inches.

The procedure which is usually used to capture the image is as follows; the HSC samples are mounted on a substrate with a gold-plated arrangement in a vacuum. After the coating, the samples are kept on the microscope for initial processing. It is mounted on the grid, and the position of samples can be adjusted in all three directions by tilting or rotation. Further, the signal is released between electrons and atoms on the HSC specimens. SEM micrographs can be captured in two methods i.e., backscattered and secondary emission. In the present study, a secondary emission model was adopted.

A field emission scanning electron microscope (FESEM) was used to envisage a small topographic detail on the surface of HSC samples (Fig. 3). This technique can be used to detect the samples even in the range of less than 1 nanometer. Microscopic examinations were made on the HSC samples with a ZEISS microscope.

The investigation was conducted on HSC samples that were exposed to elevated temperatures. After the heating and subsequent natural air-cooling process, the samples were tested to find the loss in compressive strength and further damage assessment. After the strength test, HSC samples were collected into plastic bags to conduct the SEM test. Samples of size between 3 and 4 cm were extracted from the damaged specimens without coarse aggregate. The concrete pieces were imaged by an electron microscope at 1000 magnifications. The damage levels in

the sample are quantified in terms of area, porosity percentage, and microcrack width of the specific samples. The measured mean porosity from the identified samples is used for comparing the image-based porosity.

Fig. 4 shows the high-strength fire-damaged concrete samples heated for different durations (i.e., 60/120/180 and 240 min). It is visible from the images that the pores are displayed very prominently. SEM images indicate the significant changes in the surface morphology of HSC specimens in terms of microcracks, pores, and voids, as a result of heating exposure. The SEM micrographs disclosed the characteristics and features of damaged constituent materials after thermal exposure.

Fig. 5 shows the SEM images of high-strength fire-damaged concrete samples heated for different durations (i.e., 60/120/180 and 240 min.). The SEM images are much helpful in identifying the changes due to the degradation of concrete at elevated temperatures [22]. It demonstrates the decomposition of calcium hydroxide and calcium silicate hydrate gel, with the development of cracks under the effect of temperature. Changes were noted in the structure of affected samples of HSC, the interface between the aggregate phase, and the cement paste of the exposed
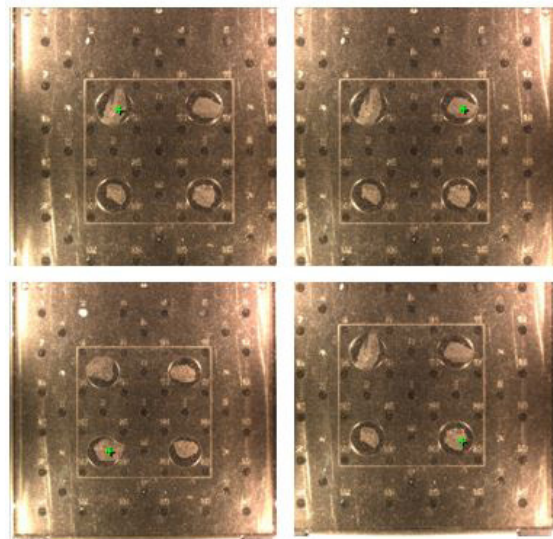
Fig. 4 Samples used for SEM analysis
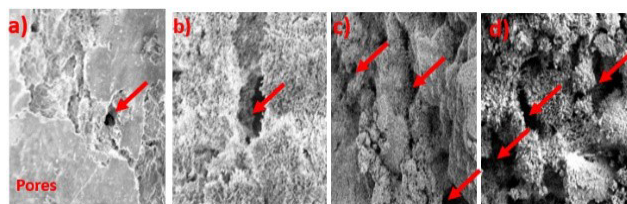
Fig. 5 SEM images of HSC exposed to Elevated temperature:
(a) 60 min, (b) 120 min (c) 180 min (d) 240 min

Fig. 3 View of FESEM used for this investigation

samples. The increase in temperature increases the quantity of microcracks in terms of length and width. Fig. 6 shows the flow diagram for pores detection.

4.1 Image processing technique

Let $I(x, y)$ be the continuous input image. The grayscale of the input image concerning the coordinates is continuous. The sampling and quantization processes are used to obtain the digital images. In the digital images, the gray colour values vary from 0 to 255. The digital SEM images are two-dimensional signals which are represented by $A \times B$ matrix. The digital images J_{xy} can be stored and analyzed in the matrix form, which is given below:

$$J(x,y) = \begin{bmatrix} J(0,0) & \cdots & J(0,B-1) \\ \vdots & \ddots & \vdots \\ J(A-1,0) & \cdots & J(A-1,B-1) \end{bmatrix}. \quad (1)$$

The prime processing blocks of digital images are pre-processing, enhancement, binarization, and thresholding.

The pre-processing step is used to remove noises that are caused by acquisition sensors, capturing the environment and humans. The SEM images are usually affected by salt and pepper noise. The median filter is used to remove the noise [23]. Due to insufficient exposure, the SEM image gray levels may be limited, which may adversely affect the determination of pores. To enhance the image quality, the enhancement step is undertaken. The main purpose is that the enhanced SEM image provides acceptable contrast and brightness. With the image enhancement step, the major and minor pores are identified well. Initially, the deficient SEM image intensities are regularized by applying Eqs. (2) and (3).

$$M(x,y) = \frac{I(x,y)}{\sqrt[\mu]{E(|I(x',y')|^\mu)}} \quad (2)$$

$$N(x,y) = \frac{M(x,y)}{\sqrt[\mu]{E\left(\min\left(\gamma, |M(x',y')|^\mu\right)\right)}} \quad (3)$$

Where $I(x, y)$ is the input image with the coordinates (x, y). $M(x, y)$ and $N(x, y)$ is the outcome images of Eqs. (2) and (3). is the compressive exponent used to reduce the effect of high values. γ is the adaptive threshold that is used to regulate very high intensities. The values of γ are 15 to 20, and the value of μ is 0.22. Even after the regularization process, extreme values of intensities exist. To avoid this and to provide suitable contrast enhancement, the following trigonometric function is applied.
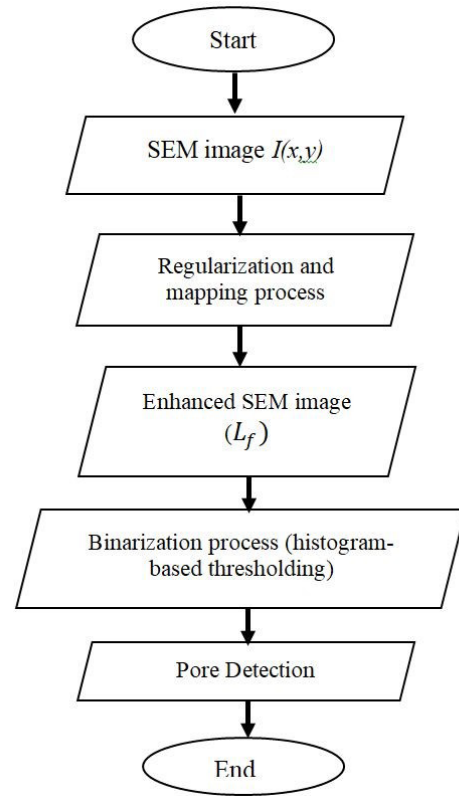
Fig. 6 Flow diagram for pore detection

$$O(x,y) = \gamma \tanh\left(\frac{N(x,y)}{\gamma}\right) \quad (4)$$

Where, $O(x, y)$ is the final resulting image. The major challenge lies in the setting of threshold values. The SEM images vary to the different heating specimens. In some images, the regularization step increases the brightness of the entire SEM images causing the essential information of the images to vanish. To customize this regularization step, the adaptive threshold values are tuned into a single threshold value as χ ($\chi > 0$). The logistic function and modified logistic function are used to control the overall brightness and contrast of the inputs (Eq. (5)).

$$L_f = \left(\frac{e^{N''(x,y)}}{1+e^{N''(x,y)}}\right)^\chi \quad (5)$$

Where L_f is the resultant image that is applied with logistic function. The resultant image has a modified contrast, and it is normalized by its maximum intensities.

After the image enhancement, the binarization step is applied to the input. It is used to identify the damage regions and their occurrence percentage. To maintain the relative consistency, the grayscale images are turned into binary images with two gray levels. The black color indicates pore damage, while the white color indicates damage-

free regions. Histogram-based thresholding is adopted to separate the grayscale images. If the gray color levels of input images are below the predefined threshold, then these are considered as the target damages, and the gray levels which are above the threshold are discarded.

4.2 Distribution of pores

After the detection of pores, the percentage of pore distribution is determined using the image volume method [24]. The total sum of porosity pixels of the input images is divided by the sum of areas of the image, and it is multiplied by 100 to determine the porosity percentage. Each fire-affected HSC specimen is imaged under various heating durations i.e., 60/120/180 and 240 min. Fifty sub-images are taken from each SEM image which produces fifty porosities using the aforesaid method. The average porosity is taken as the porosity of each specimen. The same method is also adopted for other specimens to determine the average porosity.

5 Analysis of results and discussions
5.1 Detection of pores

The SEM images were taken in the size of 128 × 128. In total, 500 images were considered in the present investigation. The image processing steps were applied to the input SEM image, and the porous regions of the images were detected. Fig. 7 shows the SEM images of the HSC specimens with various heating durations, quantified porosity, and the corresponding porous damages. The final processed images after enhancement, binarization, and thresholding are presented in the Fig. 7 where the black regions identify the pores. The porosity is the ratio of pores' pixels to the total number of pixels in the given image.

5.2 Distribution of porosity

The histogram of pore size distribution is given in Fig. 8. The SEM images were taken at a magnification of 5× and 20×. The pore size was measured in a micrometer. It can be seen from Fig. 8 that the pore size varies with the magnification scale, and the smaller pores can be detected at higher magnifications i.e., 20×. Under the two magnifications of 5× and 20×, the characteristics of pore sizes are varied.

5.3 Comparison between SEM analysis and the experimental results

The porosity of each specimen is obtained for two magnifications: 5× and 20×. Fifty sub-images are taken from each SEM image which produces fifty porosities using
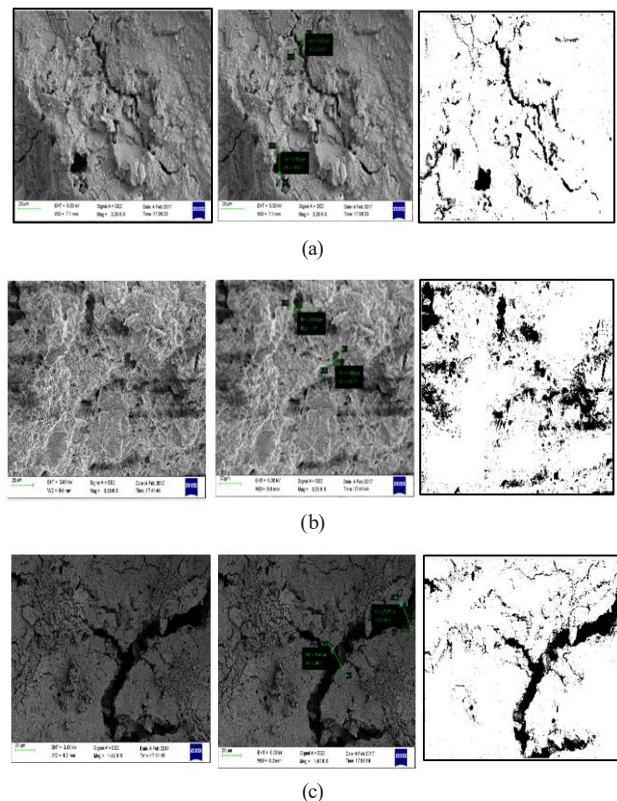
Fig. 7 Detected pores from SEM images using image processing methods (a) 60 minutes, (b) 120 minutes, (c) 180 minutes, and (d) 240 minutes

the aforesaid method. The average porosity is taken as the porosity of each specimen. The results are evaluated and compared with the mean porosity obtained from SEM analysis (FESEM results for samples of 20× magnification).

It can be seen from Fig. 7 that the image-based porosity values were lesser than the porosity obtained from the SEM results. These deviations are significant when the magnification level is high. The deviation in the digitally calculated porosities ranges between 2.55% and 5.04%, with a deviation of 3.98%. The image processing-based porosities calculation depends on the volume occupied by pores, and very few micro-pores may likely be missed out. Hence minimum deviations can occur in the image processing-based calculation.

The porosity of HSC specimens that are exposed to different durations of heating was determined during the SEM investigation based on the geometric data. The experimental SEM-based porosity (%) was obtained for all the samples during the capturing process. These results were used to compare with the predicted porosity of the respective samples, as shown in Fig. 9 for 20X magnification. Fifty positions were randomly chosen from each specimen and captured via SEM. A total of 500 images were considered for the investigation.

(a)

(b)
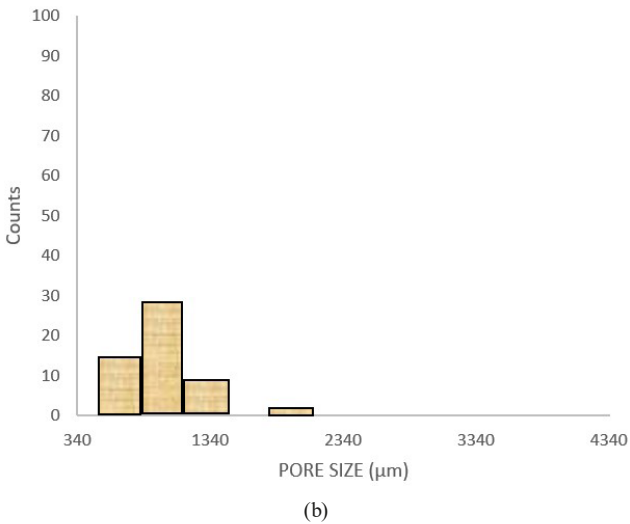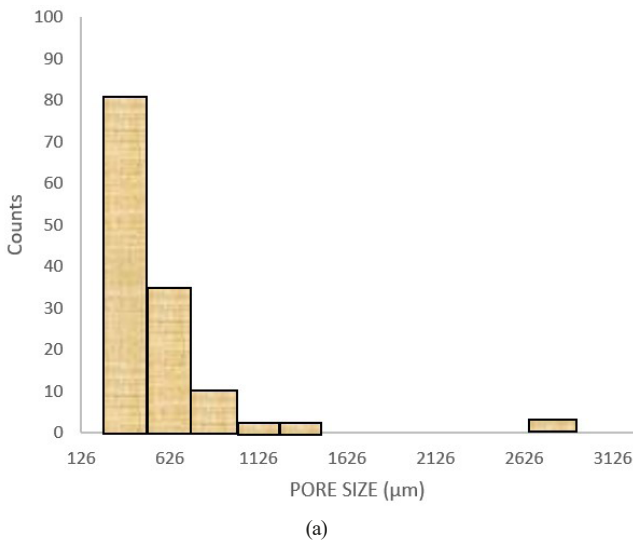
Fig. 8 Histogram of pore size distribution under
(a) 5× and (b) 20× magnification

Also, it can be seen from Fig. 9 that the percentage of deviation for the image-based method for the experimental results was in the range of 2.5% to 4.7%, 3.1% to 4.7%, 3.1% to 5.0%, and 3.2% to 4.6% for 60-, 120-, 180- and 240-min heating duration, respectively. The distribution of pores was much higher for the HSC specimens, which were kept under elevated temperature for 240 min. The percentage porosity values obtained from experimental results (SEM analysis) and SEM image-based methods also confirm the same.

The correlation between image-based porosity and experimental porosity was analyzed using the Pearson's correlation coefficient (r). This method assesses the linear relationship between two sets of parameters ranging between -1 and +1. The closer values indicate a stronger correlation. This coefficient is calculated using Eq. (6):

$$r = \frac{\sum (x - \bar{x})(y - \bar{y})}{\left(\sum (x - \bar{x})^2 \sum (y - \bar{y})^2 \right)^{\frac{1}{2}}} \tag{6}$$

Table 4 presents the correlation between SEM images based on porosity and experimental porosity (SEM analysis). The results presented in Table 4 show that there is

(a)

(b)

(c)

(d)
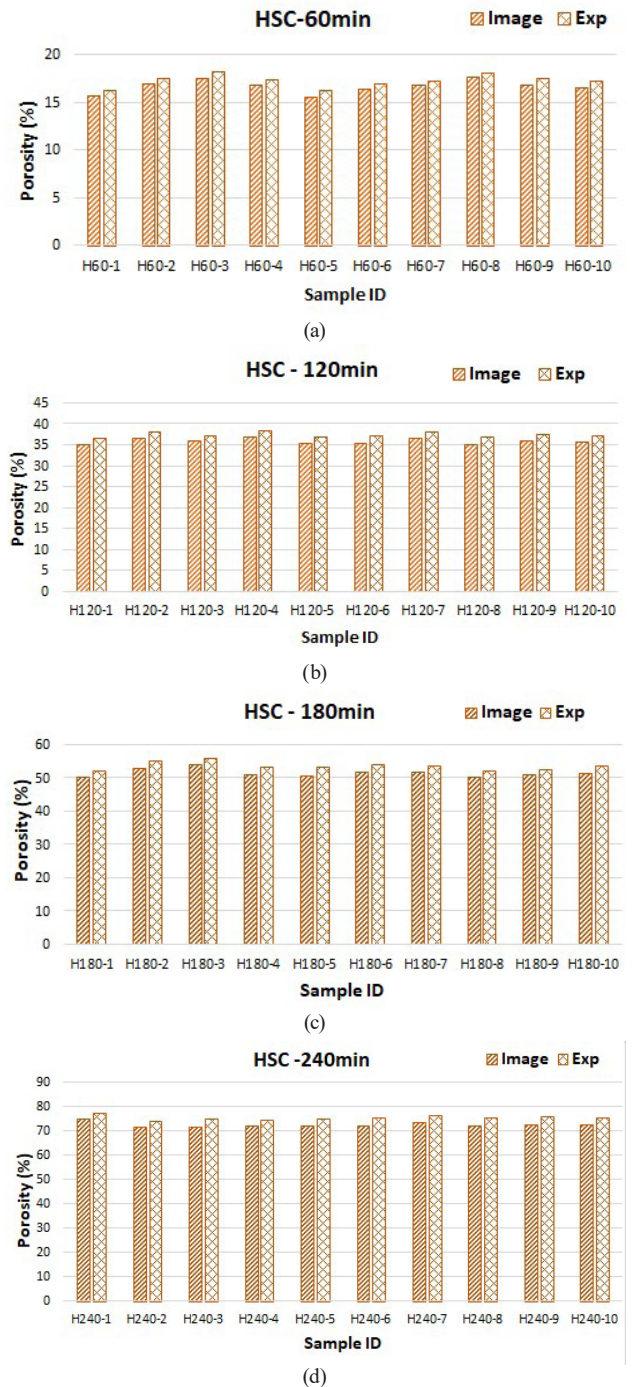
Fig. 9 Porosity values of temperature exposed HSC specimens (a) 60 min, (b) 120 min, (c) 180min, (d) 240 min
#H60-1 means, a specimen exposed to heating for 60 min and the specimen number is 1.

Table 4 Pearson's correlation coefficient values for SEM image-based porosity and experimental porosity

Type of specimen	Number of SEM images	Experimental porosity	SEM Image based porosity	Pearson correlation coefficient
HSC 60	125	0.979	0.982	0.988
HSC 120	125	0.957	0.948	0.956
HSC 180	110	0.970	0.952	0.966
HSC 240	140	0.968	0.973	0.972

a strong and consistent correlation between the two methods, and the percentage of surface porosities is strongly correlated to the specimens with different heating durations.

SEM-based porosity detection is vital in the field of structural health monitoring. The digital image processing methods of K-means and watershed segmentation were used to determine the number of voids in the SEM images. The void detection accuracy of 88% was achieved through the SEM image analysis. The geo-referenced concrete SEM images are analyzed to find the crack densities [25]. The K-means clustering method and k-centroids were leveraged to find the major elemental distribution (Si, O_2, and C). Additionally, the crack densities were measured by exaggerating the SEM images. The SEM image-based porosity detection and classifications were performed by [26] in cement-based materials. The proposed study provided reliable image analysis and conventional damage detection results. Hence, the SEM-based image analysis methods nullified the difficulty of identifying porosity on visual perception and promoting the research development in damaged concrete elements.

5.3.1 Interaction between sorptivity and porosity

The excess water in the concrete evaporates during the heating process, leaving voids and capillary pores inside the concrete paste, which are directly related to the porosity of concrete. The selection of quality ingredients and appropriate mix design are some of the key factors for producing impervious concrete. Concrete with a higher percentage of porosity absorbs water through the porous body. The cement paste contains CSH gel and pores. Effect of temperature is seen to further increases the porosity in the microstructure of concrete [27]. Porosity, sorptivity, and water permeability are some of the quantitative measurements used to estimate the magnitude of porous levels in concrete. The rate of absorption of water by capillary suction is called sorptivity of unsaturated concrete [28].

The capillary water absorption of concrete was carried out following ASTM C 1585 using cylinder samples of

35 mm in diameter and 60 mm in height. After the curing process, the samples were kept in the oven at 60 °C for a mass stabilization process. This test was carried out in such a way that the base of the cylindrical samples was under contact with water. The mass value of the test specimens was recorded at regular intervals (i.e., 5 min and up to 48-hrs). Fig. 10 shows the correlation between sorptivity and porosity from both the experimental and image-based analysis results. It is seen from Fig. 9 that as the temperature exposure increases, the sorptivity and porosity increase for the HSC specimens at different heating durations.

Fig. 10 shows a strong positive correlation between the experimental porosity, predicted image-based porosity, and sorptivity of specimens. Even though the sorptivity is the parameter measured on the surface of the specimen, it can be correlated with porosity for better understanding.

5.3.2 Factors influencing the porosity of exposed concrete

Permeability is considered a key influencing factor in examining the durability of concrete. In the present investigation, experiments were conducted to evaluate the coefficient of permeability of reference and temperature exposed concrete specimens following IS 3085 [29], as shown in Table 5.

The Co-efficient of Permeability (K) can be estimated using $Cp = \dfrac{W}{\left(\dfrac{a \times t \times h}{l}\right)}$ where, C_p = Coefficient of permeability (m/sec), W = Quantity of water percolating during the test period (mm), a = Area of the HSC specimen in m², t = time (seconds), and h/l = ratio of the pressure head to the thickness of the HSC specimen.
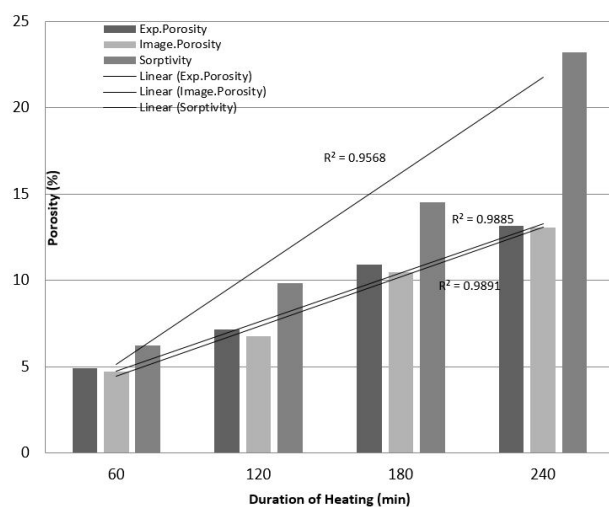
Fig. 10 Correlation between experimental and Image-based porosities for HSC at the different duration of heating

Table 5 Different key parameters/results of the experiment and analytical investigation

ID	CS (MPa)	Temp (°C)	K (m/s)	S (%)	Exp. porosity (%)	Image porosity (%)
HSC-Ref	62.2	-	$1.25 \times 10\text{-}12$	2.5	-	-
HSC 60	45.5	265	$1.625 \times 10\text{-}8$	9.2	17.2	16.6
HSC 120	22.2	670	$8.98 \times 10\text{-}3$	16.6	37.4	36.0
HSC 180	14.8	940	-	28.2	53.6	51.6
HSC 240	9.65	105	-	39.3	75.5	72.5

ID – Specimen id, CS – Compressive strength, K- Water permeability, S - Sorptivity,

The coefficient of permeability increased drastically with increasing temperatures (60 min and 120 min) compared to the reference specimen (Table 5). As the damage state of concrete is higher for the HSC 180 and HSC 240 specimens, the percolation rate was also much higher in which the exact values were not evaluated. This was due to the increased level of porosity.

Table 5 shows the experimental parameters measured for the specimens and samples. It is seen from the table that all the parameters are interrelated, and it can be concluded that a definite correlation was observed between strength and durability characteristics. The residual compressive strength is under limit state of strength criteria, whereas porosity, sorptivity, and permeability are the durability criteria for the specimens. The increase in temperature at the core has a great effect on the residual strength, porosity, and permeability of concrete. Permeability and sorptivity are measured based on the appropriate experiments for the specimens. But the porosity is measured from the SEM samples during the experiment (geometry-based) and image-based analysis. This suggests that image-based method is applicable to all types of concrete with different duration of heating. Also, this may help the engineers to evaluate the extent of damage by rigorous analysis to quantify the level of damage in terms of porosity.

5.3.3 Interaction between compressive strength, porosity, and core temperature

The correlation between strength loss, mean porosity (SEM-based), and temperature measured at the core of the specimen are shown in Fig. 11.

Fig. 12 shows the interaction graph denoting the correlation between strength loss, porosity (image-based), and temperature measured at the core of the specimen.

The porosity increases marginally at a constant rate up to 600 °C (Figs. 11 and 12). Beyond that, the porosity increases sharply at a higher rate. The initial porosity of HSC can be related to the evaporation of capillary water, adsorbed, and interlayer water. The rapid increase in porosity beyond 600 °C may be attributed to the release
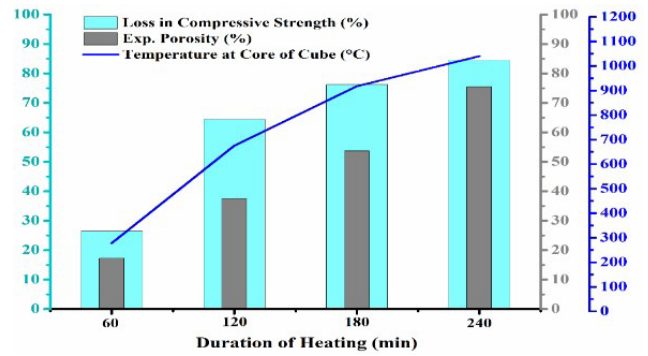
Fig. 11 Interaction graph between strength degradation, mean porosity, and temperature at the core of the specimen in blue (right axis)
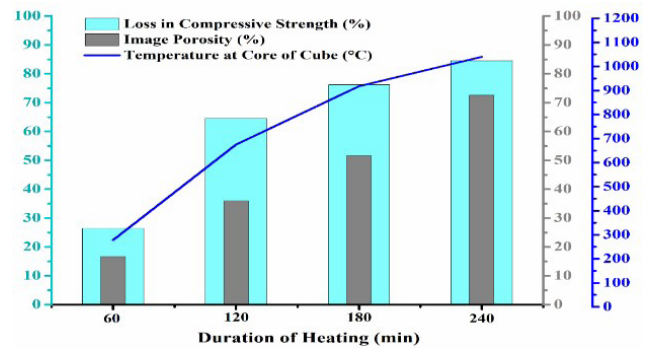
Fig. 12 Interaction graph between strength degradation, image-based porosity, and temperature at the core of the specimen in blue (right axis)

of chemically combined water due to the hydration products [30]. The increase in weight loss increases the porosity of HSC due to the effect of temperature. This weakens the microstructure by separating the bonding between the constituent materials at the interfacial transition zone (IZT) in the concrete matrix.

It is observed from figures that, from 450 °C to 850 °C, the porosity increased gradually; this is mainly due to the evaporation of free water. The loss in strength was marginal (26.2%–64.4%) during this temperature range (Figs. 11 and 12). The disintegration of $CaCO_3$ is the major factor that affects the porosity of HSC between 600 °C and 1050 °C, and the porosity reaches up to about 553.69% in this range [31]. However, a sharp increase in porosity (52% to 74%) and a decrease in compressive strength (64.4%–82.5%) were observed beyond 800 °C, confirming a severe

deterioration in the mechanical properties of HDC. In particular, regarding unheated concrete, the porosity values trebled for the concrete exposed to the temperature of 1000 °C [32]. In the present investigation, concrete with M60 grade was used with low or marginal porosity, then concrete with lower grades. However, when exposed to higher temperature exposure, high-strength concrete is more prone to weight loss and strength loss; thereby, the porosity also increases.

Increase in porosity develops the expansion between the aggregate phase and cement phase due to the increase in temperature [33]. It was mainly due to the escape of bound water and the creation of micro-cracks. Similar observations were made by [34], who concluded that the development of porosity in concrete under higher temperatures was due to the evaporation of absorbed water in capillary pores. The observation of [35] reveals that the increase in the porosity of concrete was due to the disintegration of C-S-H gel in the temperature ranges between 800–1000 °C (120 min). A similar behavior was noted in the present experiments also. In the present investigation, the SEM images at 240 minutes of fire duration showed a higher number of pores and cracks than lower durations.

SEM investigation of damaged HSC samples revealed substantial variations in the morphology of the concrete exposed to a higher temperature. The presence of micro-cracks, pores, and voids, the deformation of Calcium hydroxide crystals, and disordered calcium silicate hydrate gel are some of the features observed in HSC at elevated temperatures. Therefore, the significant loss in mechanical properties observed at higher temperatures was mainly due to the increased porosity [7].

As seen from the SEM images presented in Fig. 5, the changes that appeared in the calcium silicate hydrate gels, and their matrix at the interface are due to the effect of temperature. For the control mixture, the internal microstructure is well compacted, and the calcium silicate hydrate gels are well distributed without any disruption. As the HSC was exposed to 650 °C (less than 60 min) temperature, the internal microstructure of HSC was still compact, but the pores in the calcium hydroxide and calcium silicate hydrate gels started to increase. If the elevated temperature exceeds 800 °C (beyond 60 min), deterioration in the calcium hydroxide and calcium silicate hydrate gel appears in the internal structure of the concrete matrix. The microcracks and pores in the cement matrix and interfacial transition zone were increased with increasing temperature (180–240 min). The increase in the

number of cracks and pores caused a decrease in compressive strength [36–38]. Similar conclusions were reported in the literature [8, 9, 14, 35, 36].

The residual strength properties and damage level of HSC change with temperature exposure than those of conventional concrete. However, moisture level, the density of concrete, rate of heating and cooling, powder content, and porosity are the key influencing factors that affect the residual strength [7, 39]. Variation in the porosity with increasing temperature/duration is the key property desirable for examining the spalling of HSC [40]. The increase in temperature results higher damages in concrete such as cracks, spalling, and pores [41].

6 Conclusions

In the present investigation, following key findings have been made to analyze the porosity of HSC exposed to different elevated temperature profiles.

- The porosity percentage is calculated through SEM images. The porosity obtained from SEM image analysis is compared with experimental porosity.
- It is revealed that for both methods, the values are found in agreement with each other with the error of 3.39%, 3.93%, 3.88%, and 3.94% for 60 min, 120 min, 240 min, and 360 min heating duration, respectively.
- The surface porosity is varied for the different magnifications of SEM images. The average porosity is calculated through the digital image processing method missed out some of the micropores in the sample specimen, which is not included in the average surface porosity calculation.
- A positive correlation has been obtained among the sorptivity, experimental porosity, and image-based porosity values.
- Though this study used only HSC, it is applicable for other types of concretes, such as high dense and high-performance concrete.
- The average porosity percentage calculated using the image processing method is needed to understand better the structural behavior of porous concrete materials.
- The major limitation of the work remains that it can be done only for surface pores.

References

[1] ASTM International "ASTM C 1585-04 Standard Test Method for Measurement of Rate of Absorption of Water by Hydraulic-Cement Concretes", Annual Book of ASTM Standards, West Conshohocken, PA, USA, 2004.
https://doi.org/10.1520/C1585-04

[2] Kanagaraj, B., Anand, N., Raj, S. R., Lubloy, E. "Performance evaluation of sodium silicate waste as a replacement for conventional sand in geopolymer concrete", Journal of Cleaner Production, 375, 134172, 2022.
https://doi.org/10.1016/j.jclepro.2022.134172

[3] Ahmad, S. I., Hossain, M. A. "Water Permeability Characteristics of Normal Strength Concrete Made from Crushed Clay Bricks as Coarse Aggregate", Advances in Material Science and Engineering, 2017, 7279138, 2017.
https://doi.org/10.1155/2017/7279138

[4] Kanagaraj, B., Kiran, T., Anand, N., Al-Jabri, K., Justin, S. "Development and strength assessment of eco-friendly geopolymer concrete made with natural and recycled aggregates", Construction Innovation, 23(3), pp. 524–545, 2023.
https://doi.org/10.1108/ci-08-2021-0157

[5] Mathews, M. E., Anand, N., Kodur, V. K. R., Arulraj, P. "The bond strength of self-compacting concrete exposed to elevated temperature", Proceedings of the Institution of Civil Engineering - Structures and Buildings, 174(9), pp. 804–821, 2021.
https://doi.org/10.1680/jstbu.20.00105

[6] Don, W., Suryanto, B., Tambusay, A., Suprobo, P. "Forensic assessments of the influence of reinforcement detailing in reinforced concrete half-joints: A nonlinear finite element study", Structures, 38, pp. 689–703, 2022.
https://doi.org/10.1016/j.istruc.2022.02.029

[7] Thanaraj, D. P., Anand, N., Arulraj, G. P., Zalok, E. "Post-fire damage assessment and capacity based modeling of concrete exposed to elevated temperature", International Journal of Damage Mechanics, 29(5), pp. 748–779, 2019.
https://doi.org/10.1177/1056789519881484

[8] Armand, G., Bumbieler, F., Conil, N., de la Vaissière, R., Bosgiraud, J.-M., Vu, M.-N. "Main outcomes from in situ thermo-hydro-mechanical experiments programme to demonstrate feasibility of radioactive high-level waste disposal in the Callovo-Oxfordian claystone", Journal of Rock Mechanics and Geotechnical Engineering, 9(3), pp. 415–427, 2017.
https://doi.org/10.1016/j.jrmge.2017.03.004

[9] Chinchillas-Chinchillas, M. J., Rosas-Casarez, C. A., Arredondo-Rea, S. P., Gómez-Soberón, J. M., Corral-Higuera, R. "SEM image analysis in permeable recycled concretes with silica fume. A quantitative comparison of porosity and the ITZ", Materials, 12(13), 2201, 2019.
https://doi.org/10.3390/ma12132201

[10] Guo, L., Wang, W., Zhong, L., Guo, L., Zhang, F., Guo, Y. "Texture analysis of the microstructure of internal curing concrete based on image recognition technology", Case Studies in Construction Materials, 17, e01360, 2022.
https://doi.org/10.1016/j.cscm.2022.e01360

[11] Bahmani, H., Mostofinejad, D. "A review of engineering properties of ultra-high-performance geopolymer concrete", Developments in Built Environment, 14, 100126, 2023.
https://doi.org/10.1016/j.dibe.2023.100126

[12] Ibrahem, Y., Morozov, V. P., El-Kadi, M., Alaa, A. "Porosity enhancement potential through dolomitization of carbonate reservoirs, a case of study from the Euphrates Graben fields, East Syria", Petroleum, 9, pp. 183–198, 2021.
https://doi.org/10.1016/j.petlm.2021.05.005

[13] Miguel-Solak, A., Tenza-Abril, A. J., García-vera, V. E. "Adopting an image analysis method to study the influence of segregation on the compressive strength of lightweight aggregate concretes", Construction and Build Materials, 323, 126594, 2022.
https://doi.org/10.1016/j.conbuildmat.2022.126594

[14] Wawrzeńczyk, J., Kozak, W. "A method of analyzing the porous microstructure in air-entrained concrete on the basis on 2D image analysis", Procedia Engineering, 108, pp. 102–107, 2015.
https://doi.org/10.1016/j.proeng.2015.06.124

[15] Yoshitake, I., Maeda, T., Hieda, M. "Image analysis for the detection and quantification of concrete bugholes in a tunnel lining", Case Studies in Construction Materials, 8, pp. 116–130, 2018.
https://doi.org/10.1016/j.cscm.2018.01.002

[16] Enfedaque, A., Alberti, M. G., Gálvez, J. C., del Río, M. A., Xiaobo, T. "Use of digital image correlation to connect fracture curves and sectional analysis for structural design of polyolefin fibre reinforced concrete elements", Construction and Building Materials, 328, 127039, 2022.
https://doi.org/10.1016/j.conbuildmat.2022.127039

[17] BIS "IS 10262 Concrete Mix proportioning-Guidelines", Bureau of Indian Standards, New Delhi, India, 2019.

[18] ISO "ISO 834-1. "Fire resistance tests - elements of building construction - Part 1: General requirements", International Organization for Standardization, Geneva, Switzerland, 1999.

[19] BIS "IS 516 Method of Tests for Strength of Concrete -specifications", Bureau of Indian Standards, New Delhi, India, 2004.

[20] Kanagaraj, B., Lubloy, E., Anand, N., Hlavicka, V., Kiran, T. "Investigation of physical, chemical, mechanical, and microstructural properties of cement-less concrete – state-of-the-art review", Construction and Build Materials, 365, 13002, 2023.
https://doi.org/10.1016/j.conbuildmat.2022.130020

[21] al-Swaidani, A. M. "Use of micro and nano volcanic scoria in the concrete binder: Study of compressive strength, porosity and sulfate resistance", Case Studies in Construction Materials, 11, e00294, 2019.
https://doi.org/10.1016/j.cscm.2019.e00294

[22] Tahwia, A. M., Ellatief, M. A., Bassioni, G., Heniegal, A. M., Elrahman, M. A. "Influence of high temperature exposure on compressive strength and microstructure of ultra-high performance geopolymer concrete with waste glass and ceramic", Journal of Materials Research and Technology, 23, pp. 5681–5697, 2023.
https://doi.org/10.1016/j.jmrt.2023.02.17

[23] Li, X., Lin, H., Chen, W., Liang, S., Huang, L. "A numerical study on the tensile splitting of concrete with digital image processing", Journal of Materials Research and Technology, 25, pp. 1626–1641, 2023.
https://doi.org/10.1016/j.jmrt.2023.06.026

[24] Nazmul, I. M., Matsumoto, T. "High resolution COD image analysis for health monitoring of reinforced concrete structures through inverse analysis", International Journal Solids and Structures, 45, pp. 159–174, 2008.
https://doi.org/10.1016/j.ijsolstr.2007.07.014

[25] Ferreira, M. D. C., Venturini, W. S., Hild, F. "On the analysis of notched concrete beams: From measurement with digital image correlation to identification with boundary element method of a cohesive model", Engineering Fracture Mechanics, 78, pp. 71–84, 2011.
https://doi.org/10.1016/j.engfracmech.2010.10.008

[26] Dow, H., Perry, M., McAlorum, J., Pennada, S., Dobie, G. "Skeleton-based noise removal algorithm for binary concrete crack image segmentation", Automation in Construction, 151, 104867, 2023.
https://doi.org/10.1016/j.autcon.2023.104867

[27] Ojala, T., Ahmed, H., Kuusela, P., Seppänen, A., Punkki, J. "Monitoring of concrete segregation using AC impedance spectroscopy", Construction and Building Materials, 384, 131453, 2023.
https://doi.org/10.1016/j.conbuildmat.2023.131453

[28] Kanagaraj, B., Anand, N., Raj. R. S., Lubloy, E. "Performance evaluation on engineering properties of sodium silicate binder as a precursor material for the development of cement-free concrete", Developments in Built Environment, 12, 100092, 2022.
https://doi.org/10.1016/j.dibe.2022.100092

[29] BIS "IS:3085 Method of test for Permeability of Cement Mortar and Concrete", Bureau of Indian Standards, New Delhi, India, 2016.

[30] Galkovski, T., Mata-Falcón, J., Kaufmann, W. "Experimental investigation of bond and crack behaviour of reinforced concrete ties using distributed fibre optical sensing and digital image correlation", Engineering Structures, 292, 116467, 2023.
https://doi.org/10.1016/j.engstruct.2023.116467

[31] Zielińska, M., Rucka, M. "Internal imaging of concrete fracture based on elastic waves and ultrasound computed tomography", Measurement, 202, 111852, 2022.
https://doi.org/10.1016/j.measurement.2022.111852

[32] Kanagaraj, B., Anand, N., Andrushia, A. D., Lubloy, E. "Investigation on engineering properties and micro-structure characteristics of low strength and high strength geopolymer composites subjected to standard temperature exposure", Case Studies in Construction Materials, 17, e01608, 2022.
https://doi.org/10.1016/j.cscm.2022.e01608

[33] Abed, M., de Brito, J. "Evaluation of high-performance self-compacting concrete using alternative materials and exposed to elevated temperatures by non-destructive testing", Journal of Build Engineering, 32, 101720, 2020.
https://doi.org/10.1016/j.jobe.2020.101720

[34] Tu, W., Zhang, M. "Behaviour of alkali-activated concrete at elevated temperatures: A critical review", Cement and Concrete Composites, 138, 104961, 2023.
https://doi.org/10.1016/j.cemconcomp.2023.104961

[35] Kannangara, T., Joseph, P., Fragomeni, S., Guerrieri, M. "Existing theories of concrete spalling and test methods relating to moisture migration patterns upon exposure to elevated temperatures – A review", Case Studies in Construction Materials, 16, e01111, 2022.
https://doi.org/10.1016/j.cscm.2022.e01111

[36] Özen, S., Alam, B. "Compressive Strength and Microstructural Characteristics of Natural Zeolite-based Geopolymer", Periodica Polytechnica Civil Engineering, 62(1), pp. 64–71, 2018.
https://doi.org/10.3311/PPci.10848

[37] James, C., Sivasankarapillai, G. "Assessment of Natural Additives Modified Lime Mortars for Repair of Historic Structures with Strength, Durability and Microstructural Parameters", Periodica Polytechnica Civil Engineering, 67(1), pp. 282–297, 2023.
https://doi.org/10.3311/PPci.21135

[38] Çetintaş, S. "Investigation of Pore and Filling Material Bond in Filled Travertine Used as a Building Material", Periodica Polytechnica Civil Engineering, 67(1), pp. 80–92, 2023.
https://doi.org/10.3311/PPci.20845

[39] Kim, H.-T., Park, K. "Computed tomography (CT) Image-based analysis of concrete microstructure using virtual element method", Composite Structures, 299, 115937, 2022.
https://doi.org/10.1016/j.compstruct.2022.115937

[40] Kanagaraj, B., Anand, N., Andrushia, A. D., Kiran, T., Lubloy, E. "Pull-Out behavior and microstructure characteristics of binary blended self-compacting geopolymer concrete subjected to elevated temperature", Alexandria Engineering Journal, 76, pp. 469–490, 2023.
https://doi.org/10.1016/j.aej.2023.06.055

[41] Andrushia, A. D., Anand, N., Arulraj, G. P. "Evaluation of thermal cracks on fire exposed concrete structures using Ripplet transform", Mathematics and Computers in Simulation, 180, pp. 93–113, 2021.
https://doi.org/10.1016/j.matcom.2020.07.024